Anomalous helicity-dependent photocurrent in the topological insulator (Bi_{0.5}Sb_{0.5})_{2}Te_{3} on a GaAs substrate

Dong-Xia Qu, Xiaoyu Che, Xufeng Kou, Lei Pan, Jonathan Crowhurst, Michael R. Armstrong, Jonathan Dubois, Kang L. Wang, and George F. Chapline

Phys. Rev. B **97**, 045308 — Published 24 January 2018

DOI: 10.1103/PhysRevB.97.045308

Anomalous helicity-dependent photocurrent in topological insulator $(Bi_{0.5}Sb_{0.5})_2Te_3$ on GaAs substrate

Dong-Xia Qu[1], Xiaoyu Che[2], Xufeng Kou[2], Lei Pan[2], Jonathan Crowhurst[1], Michael R. Armstrong[1], Jonathan Dubois[1], Kang L. Wang[2] and George F. Chapline[1]

[1]*Lawrence Livermore National Laboratory, Livermore, California 94550, USA*

[2]*Department of Electrical Engineering,*

University of California, Los Angeles, California 65409, USA

(Dated: January 12, 2018)

The emerging material, topological insulator, has provided new opportunities for spintronic applications, owing to its strong spin-orbit character. Topological insulator based heterostructures that display spin-charge coupling driven by topology at surfaces have great potential for the realization of novel spintronic devices. Here, we report the observation of anomalous photogalvanic effect in $(Bi_{0.5}Sb_{0.5})_2Te_3$ thin films grown on GaAs substrate. We demonstrate that the magnitude, direction, and temperature dependence of the helicity-dependent photocurrent (HDPC) can be modulated by the gate-voltage. From spatially resolved photocurrent measurements, we show that the line profile of HDPC in $(Bi_{0.5}Sb_{0.5})_2Te_3$/GaAs is unaffected by the variation of beam size, in contrast to the photocurrent response measured in a $(Bi_{0.5}Sb_{0.5})_2Te_3$/Mica structure.

I. INTRODUCTION

One of the recent advances in spintronics is the development of non-magnetic systems for a functional spintronic technology without the application of magnetic fields[1–3]. The primary driving force of this research direction is the relativistic spin-orbit coupling that links an electron's momentum to its spin, and has led to a variety of new device paradigms, such as spin Hall effect transistors[2], spin-orbit torque memories[4], and broadband terahertz emitters[5]. Topological insulator (TI), a new class of quantum state of matter, is a promising material for spintronic devices owing to its exceptionally strong spin-orbit coupling[6–12].

One manifestation of strong spin-orbit coupling in a TI is the circular photogalvanic effect

(CPGE). This effect is the appearance of a DC electrical current under circularly polarized light as a result of the optical spin orientation of free carriers. Optical experiments so far have focused on the photogalvanic current measurements in TIs via the inverse Edelstein effect (IEE), in which a circular photocurrent (J_C) arises from the asymmetrical spin accumulation in momentum space and the spin-momentum locking mechanism[13–19]. However, recent theoretical calculations predict that the surface photocurrent arising from the IEE is small, suggesting a limited spin-to-charge conversation efficiency[15]. Therefore, it is interesting to search for new device structures to enhance the spin current generation. Here, we report that the generation of HDPC in a TI is substrate dependent and gate tunable under near infrared radiation. Our work suggests that substrate material may provide a new order of freedom to influence the photon-spin conversion efficiency.

II. RESULTS

A. Experimental Details

The samples used in this study are 6∼10 quintuple layers (QLs) of single-crystalline $(Bi_{0.5}Sb_{0.5})_2Te_3$ (BST) films, grown on semi-insulating GaAs (111)B or muscovite mica substrate by molecular beam epitaxy. The growth is monitored in-situ by reflection high-energy electron diffraction (RHEED) and the thickness of the film is inferred from the RHEED oscillation periods. A 2 nm Al protective layer is deposited immediately after the TI growth. The Bi:Sb ratio is adjusted to fine tune the Fermi level[20–22], so that it lies close to the Dirac point E_D for 10-QL BST/GaAs[20]. The 10-QL BST/GaAs sample is p-type, whereas the 6-QL BST/GaAs and 6-QL BST/Mica samples are n-type. The thin films are photolithographically patterned into Hall bar structures 130 μm long and 20 μm wide, with electrical contacts made from 10 nm Cr and 100 nm Au (Fig. 1, a and b).

The scanning photocurrent measurements are carried out with a liquid helium cooled probe station (Janis ST-500), in which a three-axis piezo-based nanopositioner (Attocube ANPxyz101/RES) is mounted on the cold finger in vacuum. The device is mounted onto the nanopositioner and obliquely illuminated with a thulium continuous-wave fiber laser beam (2.036 μm, IPG Photonics) chopped at a frequency of 238 Hz. The incident angle is $\theta = 30^\circ$ from the positive z axis (Fig. 1a). The photon energy (0.609 eV) is chosen to be

much smaller than the band gaps of GaAs (1.42 eV) and Mica (7.85 eV). Hence, optical absorption primarily occurs in BST (Appendix A). To accurately read the temperature of the sample, we anchor a silicon sensor in close proximity to the substrate of the device. The polarization of the linearly polarized excitation beam is modulated by rotating a quartz $\lambda/4$ waveplate with a period from right-circularly polarized Ω^-, to linearly polarized $\leftrightarrow$, to left-circularly polarized Ω^+, and back to linearly polarized $\leftrightarrow$. The beam is consequently focused through an objective with a numerical aperture of 0.24 (Mitutoyo, 5X), which focuses the laser beam to a circular spot with a full width at half-maximum of 104 μm. The reflected light from the sample is imaged using a CCD camera, which allows us to locate the spot position. Electrical transport measurements are conducted using a pre-amplifier (SR570), a lock-in amplifier (SR830), and a digital source meter (Keithley 2400), while illuminating the device at various temperatures.

B. Helicity-dependent photocurrent in TI/GaAs and TI/Mica

We first measured the unbiased photocurrent $J_{\rm y}$ as a function of light polarization performed in the linear regime with a low laser intensity I (Appendix B). In Fig. 1, c and d, we plot the raw traces of $J_{\rm y}/I$ versus photon polarization (black circles) in the 6-QL BST/GaAs sample G1 at position $y = -65$ μm, corresponding to the edge of the channel (red triangle in Fig. 1b), and 6-QL BST/Mica sample M1 at $y = -36$ μm (black triangle in Fig. 1b), respectively. We set the origin of our coordinate system as the center of the channel. The data can be well fit to

$$J_{\rm y}(\alpha) = J_{\rm C}\sin 2\alpha + J_{\rm L1}\sin 4\alpha + J_{\rm L2}\cos 4\alpha + J_{\rm D} \tag{1}$$

where α is the angle between the polarization direction of incident light and the optical axis of the $\lambda/4$ waveplate, $J_{\rm C} = (J_{\Omega^+} - J_{\Omega^-})/2$ the amplitude of circular photocurrent that is helicity-dependent, $J_{\rm L1}$ and $J_{\rm L2}$ the amplitudes of linear photocurrents that depend on the linear polarization of the light, and $J_{\rm D}$ the amplitude of the polarization independent photocurrent that primarily comes from the thermoelectric effect. In the vicinity of the contacts, the extracted circular-photocurrents $J_{\rm C}$ are opposite in sign for samples G1 and M1 (blue curves), whereas their two-dimensional (2D) photocurrent profiles are similar in response to linearly polarized light (Fig. 1, e and f). The sign of $J_{\rm C}$ in M1 agrees with

the expectation of IEE-induced photocurrent J_{IEE} on top surface, whereas J_{C} in G1 near the electrode displays an anomalous opposite sign. For photogalvanic currents arising from the IEE, there is a partial cancellation between the spin currents generated at the top and bottom surfaces due to their opposite spin helicities. Generally, J_{IEE} on top surface is expected to be larger than that on bottom surface due to the absorption of bulk with an absorption coefficient of 2.25×10^4 cm^{-1}, which leads to reduced light intensity reaching the bottom surface[13,16,18].

We next map out the one-dimensional spatial profile of J_{C} along y axis by repeating light polarization scans at each position in samples G1, M1, and a 10-QL BST/GaAs p-type sample G2 (Fig. 1g). For sample M1, J_{C} is negative and falls off quickly towards the electrode. For sample G1, J_{C} is negative at the center and rapidly changes sign when approaching the contacts. For sample G2, J_{C} is positive throughout the channel and reaches a maximum at the BST-electrode interface. In the middle of the channel, the opposite current response in G1 and G2 might be related to the thickness-dependent binding energies of E_{D}. Angel resolved photoemission spectroscopy (ARPES) experiments found that E_{D} at 6 QLs is lower by ~ 0.1 eV than that of the 10-QL TI films[24]. It is worth noting that the current electrode may induce an upward band bending occurring in both M1 and G1 samples, leading to a Dirac point energy shift relative to Fermi energy E_{F}. The display of maximum peak J_{C} near the electrodes in both G1 and G2 implies that J_{C} is sensitive to band-bending in BST/GaAs. However, interpretation of photocurrent response near the contact can be complicated by the presence of fringe field and laser-induced heating[25]. We therefore should focus on the measurements performed at the center of the channel where the local fringe field and sample heating effects are minimized.

C. Top-gated TI/GaAs structure

Bearing this in mind, we then measured the dependence of photocurrent on the gate voltage V_{G}, because gating can tune E_{F} relative to E_{D}. Our top-gate device is prepared by fabricating a semitransparent 10 nm Ni electrode on top of a 20 nm Al_2O_3 insulated 8-QL BST/GaAs sample (Fig. 2a). Figure 2b shows the traces of J_{y}/I versus photon polarization at the center of the channel, while stepping V_{G} from -3 to 12 V. We find that both magnitude and extrema of J_{y}/I strongly depend on V_{G}, and the polarity of J_{C} can be

completely switched as the external gate field is increased.

The extracted $J_{\rm C}$, $J_{\rm D}$, $J_{\rm L1}$, and $J_{\rm L2}$ versus $V_{\rm G}$ are summarized in Fig. 2, c and d, measured for two samples S1 and S2, in which the applied gate voltage $V_{\rm G}$ changes $J_{\rm C}$ from negative to positive at $V_{\rm G0} = 2$ and 4 V, respectively. The expanded view in Fig. 2, e and f, reveals that $J_{\rm C}$ increases linearly versus $|V_{\rm G} - V_{\rm G0}|$ ($V_{\rm G} < V_{\rm G0}$) and the slopes decrease as temperature T is raised from 26 to 250 K. For $V_{\rm G} > V_{\rm G0}$, $J_{\rm C}$ tends to reach a constant value (Appendix C, Fig. 8, a and b).

D. Spatially-resolved photocurrent response in BST/GaAs and BST/Mica

To further characterize the anomalous photogalvanic current in BST/GaAs, we measured the spatially-resolved photocurrent in BST/GaAs in comparison with BST/Mica samples. The 2D images of our top-gate BST/GaAs sample show a homogeneous photocurrent response under the gate at $V_{\rm G} = 0$ V (Fig. 3, a-d) in $J_{\rm C}$, $J_{\rm D}$, $J_{\rm L1}$, and $J_{\rm L2}$. For BST/Mica, all the photocurrent components display dispersive profiles at the center of the channel (Fig. 3, e-h). When the light spot moves up to the area between the two Hall leads, $J_{\rm C}$ reverses sign from negative to positive for $x > 20$ μm (Fig. 3e). The dispersive circular photocurrent in BST/Mica might be explained as a result of the spin induced charge current whirling around the center of the light spot. Similar effect has been reported in $Al_xGa_{1-x}N$/GaN heterostructures[23]. Under the inclined incidence of a Gaussian laser beam, an inhomogeneous spin density can be excited in TI and has a non-zero z component. The gradient of the spin density generates a radial spin current J_s on the plane, which leads to a swirly charge current via the inverse spin Hall effect (ISHE) as $\boldsymbol{J}_{ISHE} \propto -\boldsymbol{J}_s \times \mathbf{P}$, where $\mathbf{P}$ is the spin angular momenta.

Another approach to modulate the lateral spin density distribution is through varying the light spot radius r. We find that the line profile of $J_{\rm C}/I$ remains nearly unchanged with decreasing r in a 10-QL BST/GaAs sample (Fig. 4, a-c, and Appendix D), whereas varies dramatically in a 6-QL BST/Mica sample. It is possible that for BST/Mica the in-plane spin transport occurs, leading to a r dependent $J_{\rm C}/I$ that reverses sign by moving the light spot along x-axis, which is the direction transverse across the channel (Fig. 4d). Additionally, for BST/Mica $J_{\rm C}(x)$ closely follows the trend of $\frac{dJ_{\rm L1}(x)}{dx}$ as shown in Fig. 4, e-f. Since $J_{\rm L1}(x)$ reflects the light intensity distribution, the derivative relation between $J_{\rm C}$ and $J_{\rm L1}$ suggests

that the dispersive J_C profile is caused by the swirly charge current.

E. Temperature dependence of photocurrent in TI/GaAs and TI/Mica structures

We next investigate the dependence of photogalvanic current with temperature in TI/GaAs and TI/Mica structures. We first look at how J_C/I varies as a function of T at each V_G in TI/GaAs. In Fig. 5, a and b, we plot J_C/I and J_D/I versus T in sample S1 at $V_G = 0$ and -3 V, respectively. In both cases, J_D/I decreases slightly as T increases from 60 to 200 K, consistent with previous observation of bulk thermoelectric photocurrent[16]. For $V_G = 0$ V, J_C/I displays a strong dependence on T, which fits well to the power-law variation $T^{-\alpha}$ ($\alpha = 1$) from 65 to 270 K (Fig. 5a). By contrast, for $V_G = -3$ V, J_C/I is nearly T independent (Fig. 5b). The different T-dependent behavior of J_C at $V_G = 0$ and -3 V implies that they may come from different origins.

Moreover, we find that the power-law scaling of J_C remains valid when the BST thin film decreases down to 6 QLs in BST/GaAs, whereas not observed in the BST/Mica sample (Fig. 5, d and e). Fig. 5c shows the line scan of J_C/I in sample G1 at $T = 61$ and 297 K. In the middle of the channel, J_C displays a sign reversal as T is lowered. We can fit J_C versus T to the power-law scaling $J_C \propto T^{-\alpha}(\alpha = 1)$ between 60-235 K (Fig. 5d). In the 6-QL BST/Mica sample M2, J_C mildly changes with T between 60 and 210 K (Fig. 5e), as commonly observed in devices of TI on insulating substrates.

III. DISCUSSION

To reveal the origin of the anomalous HDPC in BST/GaAs structure through a theoretical approach remains to be a challenge. A recent CPGE experiment[26] demonstrates that HDPC could reverse sign with a photon excitation of 1.51 eV while tuning the Fermi energy, due to the asymmetric optical transitions between surface and bulk states. It would be interesting to test whether this model could explain the different behavior of the spatially resolved HDPC between BST/GaAs and BST/Mica samples (Figs. 3 and 4).

Another possible explanation is the interface spin transport from BST to GaAs. Recently, a magnetic field-dependent CPGE measurement[27] reveals the spin injection from GaAs to TI for a Bi_2Te_3/GaAs heterostructure. We speculate that a vertical spin current

may also occur at the BST/GaAs interface and induce a charge current via the ISHE in a TI. However, it should be pointed out that as the electron affinity of BST in MBE-grown BST/GaAs is currently unavailable, the band structure at the interface of BST and GaAs cannot be accurately determined. Further studies, such as work function measurements at the BST/GaAs interface, tuning the Fermi level in BST/Mica through electrical gating, and extending measurements into low energy optical excitations, could help to identify the origin of the anomalous photocurrent.

In conclusion, we report the observation of anomalous photogalvanic current in BST/GaAs samples. Experimental evidence for such a substrate dependent anomaly is provided through gating experiments, spatially resolved photocurrent measurements, and temperature dependent photocurrent measurements. We demonstrate that the HDPC in BST/GaAs displays different direction and magnitude as a function of gate voltage, beam size, and temperature compared with those in BST/Mica. The results suggest that alternative substrate may lead to a new mechanism and possible improvement in the spin photocurrent generation. We hope our experimental work will provide important clues for developing a theory of substrate-dependent CPGE in a topological insulator/semiconductor heterostructure.

Acknowledgement

We would like to thank Yu Pan, N. Samarth, Yasen Hou, and Dong Yu for insightful discussion. This work is supported by the Department of Energy, Laboratory Directed Research and Development funding, under contracts 15-LW-018 and 16-SI-004.

Appendix A LATERAL GAAS-TI-GAAS SAMPLE

To confirm the measured photocurrent predominantly comes from the topological insulator rather than the GaAs substrate, we fabricated the lateral GaAs-TI-GaAs control sample. Figure 6a presents the optical image of a typical device. The 6-QL BST channel is connected with the current electrodes through the 5-μm-long GaAs substrate to enable the measurement of possible charge transport in the substrate.

We first characterized the devices with the linearly polarized light. Figure 6b shows

the two-dimensional image of the photocurrent J_y measured at room temperature. The photocurrent displays a polarity reverse across the sample with a maximum at the GaAs/electrode interface, which can be attributed to a thermoelectric current arising from the photoexcitation of the in-gap EL_2 impurity states in GaAs[28–32]. When the laser spot sweeps along the x axis close to the current electrode (white dotted line, Fig. 6b), J_y exhibits a peak at $x = 0$ (Fig. 6c) and the extracted J_C/I is on the order of 1 pA kW cm^{-2} that is 10× smaller than the value measured in sample G1 (Fig. 1g). We then conclude that the circular photocurrent response from GaAs substrate is negligible.

Appendix B LASER INTENSITY DEPENDENCE OF PHOTOCURRENT

In scanning photocurrent measurements, laser heating may cause photocurrent to deviate from the linear dependence on the laser intensity I. We confirmed that our photocurrent measurements are performed in the low intensity linear regime. Figure 7 shows the laser intensity dependence of the amplitude J_C, J_{L1}, J_{L2}, and J_D, fitted to the Eq. (1) in a 8-QL BST/GaAs sample at $T = 30$ K. All these four photocurrent components increase linearly with the laser intensity up to $I = 1.1$ kWcm^{-2}, below which the laser heating is minimized. We have carried out all the measurements with a low laser intensity $I < 0.85$ kWcm^{-2}.

Appendix C PHOTOCURRENT MAP IN TOP-GATE TI/GAAS DEVICES UNDER POSITIVE GATE VOLTAGE

In the top-gate samples S1 and S2, J_C varies linearly as a function of $|V_G|$ ($V_G < V_{G0}$) (Fig. 2, e and f). However, J_C is nearly invariant at $V_G > V_{G0}$ (Fig. 8, a and b). Theoretical studies have shown that surface photogalvanic current is constant as long as the chemical potential lies between the energies of the two states involved in the transition[15]. In our sample, the Fermi energy E_F increases by 27 meV as V_G is changed from 2 to 11 V. At $V_G = 11$ V, the Fermi energy is $150 \sim 250$ meV, which still lies below the upper transition state, so that surface J_{IEE} is expected to be saturate with increasing V_G up to 11 V.

In Fig. 8c, we show that J_C becomes less homogeneous at a large positive gate voltage, as revealed by the 2D scanning photocurrent image in sample S1 at $V_G = 8$ V. Under the gate electrode, J_C/I displays a weak negative signal that fluctuates in the range of $-30 \sim 2$ pA

$kW^{-1}cm^2$. This implies that there are competing mechanisms. In the gap region between the gate electrode and current contacts, J_C exhibits similarity to the profile measured at zero-gate voltage (Fig. 4e), showing a sign reversal as the laser intensity changes abruptly. The 2D photocurrent images are also mapped out for J_D, J_{L1}, and J_{L2} in Fig. 8, d-f. We observe that J_D and J_{L1} show similar profiles to the current response taken at $V_G = 0$ V, whereas J_{L2} reverses direction for opposing gate field directions.

Appendix D PHOTOCURRENT RESPONSE IN THE 10-QL BST/GAAS SAMPLE

In Fig. 9, a and b, we show the line scan of J_y along y-axis in p-type 10-QL BST/GaAs sample G2, illuminated by a linearly polarized beam with the spot radius $r = 52$ and 8.6 μm, respectively. In both cases, the photocurrent J_y peaks at the channel-contact junctions with a sign reversal across the channel, which arises from the light heating induced thermoelectric effect. The polarity of the photocurrent corresponds to the hole-like carriers that is consistent with the Hall measurement.

Figure 9c shows the raw data of J_y/I versus photon polarization (open black circles) at the edge of the channel. The extracted J_C/I versus photon polarization (blue curves) displays positive amplitude. In Fig. 9d, we plot the line profile of J_C/I against y-axis in sample G2 with a beam size ($r = 8.6$ μm) much smaller than the channel length. We find that the profile of J_C/I is almost invariant with beam size, suggesting the Gaussian beam intensity does not affect the generation mechanism of J_C in BST/GaAs. Compared to n-type BST/GaAs sample G1, J_C/I in p-type sample G2 displays a maximum at the BST-contact interface and reaches a positive plateau in the middle of the channel.

[1] Y. K. Kato, R. C. Myers, A. C. Gossard, and D. D. Awschalom, *Science* **306**, 1910 (2004).

[2] J. Wunderlich, B.-G. Park, A. C. Irvine, L. P. Zârbo, E. Rozkotová, P. Nemec, V. Novák, J. Sinova, T. Jungwirth, *Science* **330**, 1801 (2010).

[3] T. Jungwirth, J. Wunderlich, and K. Olejnik, *Nat. Mater.* **11**, 382 (2012).

[4] Y. Kim, X. Fong, K.-W. Kwon, M.-C. Chen, and K. Roy, *IEEE Trans. Electron Devices* **62**, 561 (2015).

[5] T. Kampfrath, M. Battiato, P. Maldonado, G. Eilers, J. Nötzold, S. Mährlein, V. Zbarsky, F. Freimuth, Y. Mokrousov, S. Blügel, M. Wolf, I. Radu, P. M. Oppeneer, and M. Münzenberg, *Nat. Nano.* **8**, 256-260 (2013).

[6] M. Z. Hasan and C. L. Kane, *Rev. Mod. Phys.* **82**, 3045 (2010).

[7] X.-L. Qi and S.-C. Zhang, *Rev. Mod. Phys.* **83**, 1057 (2011).

[8] D. Pesin and A. H. MacDonald, *Nat. Mater.* **11**, 409 (2012).

[9] D.-X. Qu, Y. S. Hor, J. Xiong, R. J. Cava, and N. P. Ong, *Science* **329**, 821 (2010).

[10] C. H. Li, O. M. J. van′t Erve1, J. T. Robinson, Y. Liu, L. Li, and B. T. Jonker, *Nat. Nano.* **9**, 218 (2014).

[11] P. Wei, F. Katmis, B. A. Assaf, H. Steinberg, P. Jarillo-Herrero, D. Heiman, and J. S. Moodera, *Phys. Rev. Lett.* **110**, 186807 (2013).

[12] Y. Shiomi, K. Nomura, Y. Kajiwara, K. Eto, M. Novak, K. Segawa, Y. Ando, and E. Saitoh, *Phys. Rev. Lett.* **113**, 196601 (2014).

[13] K. N. Okada, N. Ogawa, R. Yoshimi, A. Tsukazaki, K. S. Takahashi, M. Kawasaki, and Y. Tokura, *Phys. Rev. B* **93**, 081403(R) (2016).

[14] P. Hosur, *Phys. Rev. B* **83**, 035309 (2011).

[15] A. Junck, G. Refael, and F. van Oppen, *Phys. Rev. B* **89**, 075144 (2013).

[16] J. W. McIver, D. Hsieh, H. Steinberg, P. Jarillo-Herrero, and N. Gedik, *Nat. Nano.* **7**, 96 (2012).

[17] J. Duan, N. Tang, X. He, Y. Yan, S. Zhang, X. Qin, X. Wang, X. Yang, F. Xu, Y. Chen, W. Ge, and B. Shen, *Sci. Rep.* **4**, 4889 (2014).

[18] C. Kastl, H. Karl, and A. W. Holleitner, *Nat. Commun.* **6**, 7645 (2015).

[19] K. Shen, G. Vignale, and R. Raimondi, *Phys. Rev. Lett.* **112**, 096601 (2014).

[20] L. He, X. Kou, M. Lang, E. S. Choi, Y. Jiang, T. Nie, W. Jiang, Y. Fan, Y. Wang, F. Xiu, and

K. L. Wang, *Sci. Rep.* **3**, 3406 (2013).

[21] J. Zhang, C.-Z. Chang, Z. Zhang, J. Wen, X. Feng, K. Li, M. Liu, K. He, L. Wang, X. Chen, Q.-K. Xue, X. Ma, and Y. Wang, *Nat. Comm.* **2**, 574 (2011).

[22] D. Kong, Y. Chen, J. J. Cha, Q. Zhang, J. G. Analytis, K. Lai, Z. Liu, S. S. Hong, K. J. Koski, S.-K. Mo, Z. Hussain, I. R. Fisher, Z.-X. Shen, and Y. Cui, *Nat. Nano.* **6**, 705 (2011).

[23] X. W. He, B. Shen, Y. H. Chen, Q. Zhang, K. Han, C. M. Yin, N. Tang, F. J. Xu, C. G. Tang, Z. J. Yang, Z. X. Qin, G. Y. Zhang, and Z. G. Wang, *Phys. Rev. Lett.* **101**, 147402 (2008).

[24] Y. Zhang, K. He, C.-Z. Chang, C.-L. Song, L.-L. Wang, X. Chen, J.-F. Jia, Z. Fang, X. Dai, W.-Y. Shan, S.-Q. Shen, Q. Niu, X.-L. Qi, S.-C. Zhang, X.-C. Ma, and Q.-K. Xue, *Nat. Phys.* **6**, 584 (2010).

[25] J. Park, Y. H. Ahn, C. R.-Vargas, *Nano Lett.* **9**, 1742 (2007).

[26] Y. Pan, Q.-Z. Wang, A. L. Yeats, T. Pillsbury, T. C. Flanagan, A. Richardella, H. Zhang, D. D. Awschalom, C.-X. Liu, and N. Samarth, *Nature Commun.* **8**, 1037 (2017).

[27] Y. Q. Huang, Y. X. Song, S. M. Wang, I. A. Buyanova, and W. M. Chen, *Nature Commun.* **8**, 15401 (2017).

[28] J. C. Bourgoin and T. Neffati, *Solid State Electron* **43**, 153 (1999).

[29] U. V. Desnica, D. I. Desnica, and B. Santic, *Appl. Phys. Lett.* **58** , 278 (1991).

[30] J. Dabrowski and M. Scheffler, *Phys. Rev. B* **40**, 10391 (1989).

[31] M. O. Manasreh and B. C. Covington, *Phys. Rev. B* **35**, 2524-2527 (1987).

[32] J. Shah and Y. Yacoby, *Phys. Rev.* **174**, 932 (1968).

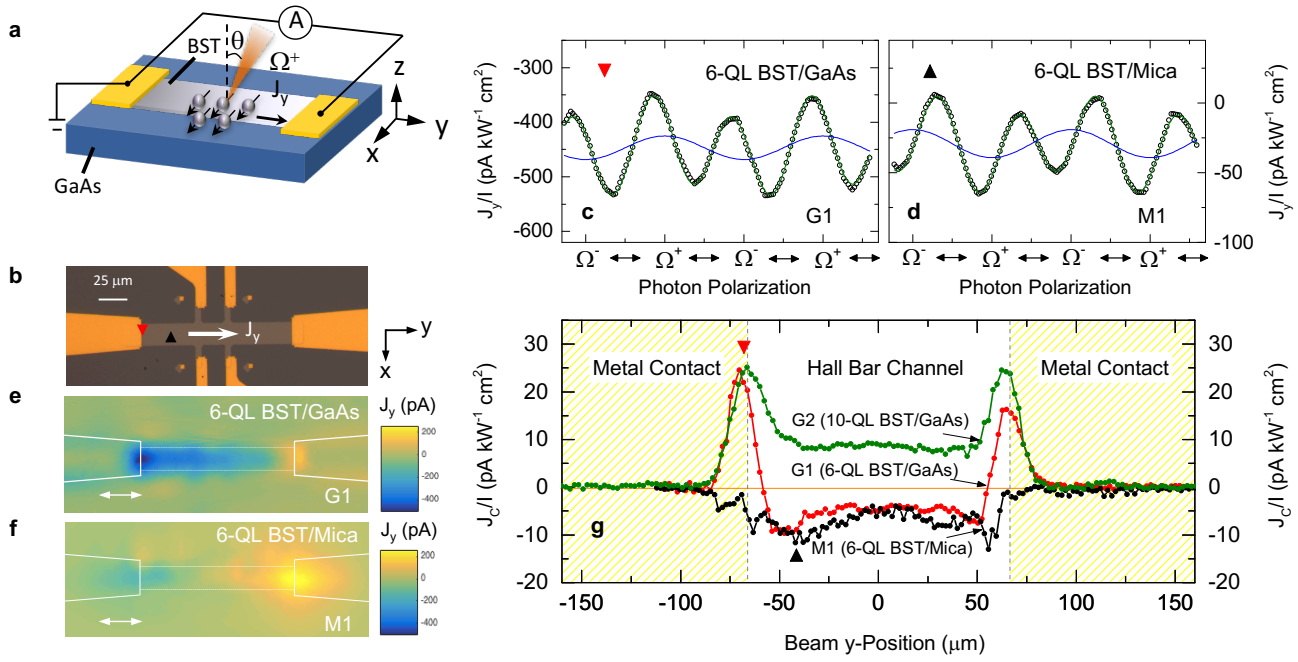

FIG. 1: Sample geometry and results of scanning photocurrent measurements. (a) Schematic of the experimental geometry. (b) The optical image of a representative BST/GaAs sample patterned into a Hall bar structure. The red (black) triangle marks the laser excitation position in sample G1 (M1) with the corresponding J_y/I shown in panel c (panel d). (c-d) J_y/I versus photon polarization for sample G1 at $y = -65$ μm (c) and sample M1 at $y = -36$ μm (d). The polarization of the light is modulated with a period from right-circularly polarized Ω^-, to linearly polarized $\leftrightarrow$, to left-circularly polarized Ω^+, and back to linearly polarized $\leftrightarrow$. The solid green lines are fits as explained in text. The solid blue curve is extracted circular photocurrent component $J_C = C \sin 2\alpha$. (e-f) Scanning photocurrent images for sample G1 (e) and M1 (f) under linearly polarized light. Dashed and solid lines indicate the edges of the sample and electrodes. (g) Spatial profiles of J_C/I along y axis for samples G1, M1, and G2 at room temperature.

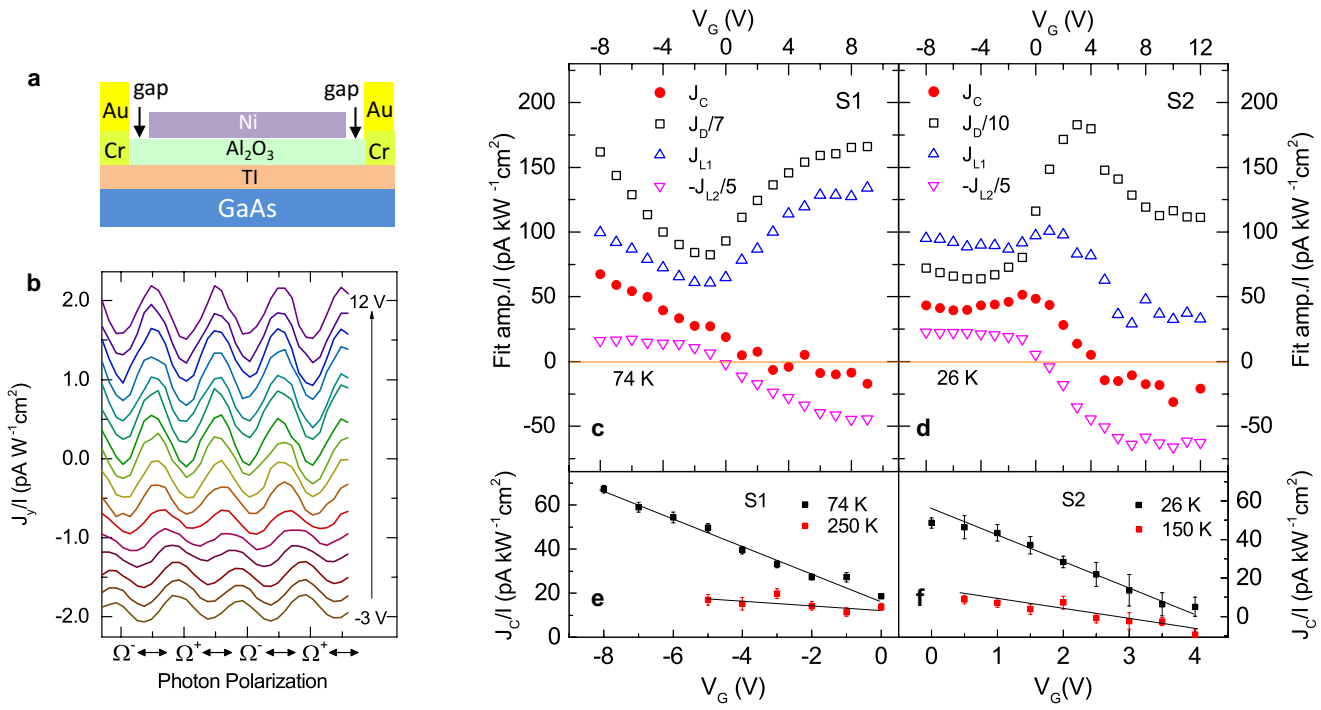

FIG. 2: Gate controllable photocurrent generation in TI/GaAs. (a) Schematic of the device structure with a top gate. (b) J_y/I as a function of photon polarization and gate voltage V_G at the center of the channel in sample S2. The curves are vertically offset for clarity. (c-d) Extracted photocurrent components as a function of V_G for samples S1 (c) and S2 (d). (e) V_G dependence of J_C/I in sample S1 at $T = 74$ and 250 K. (f) V_G dependence of J_C/I in sample S2 at $T = 26$ and 150 K.

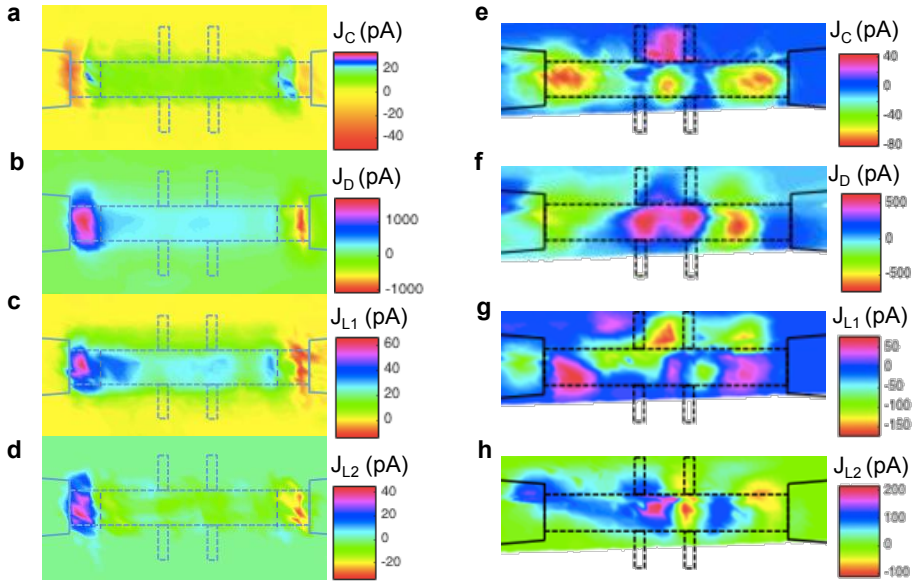

FIG. 3: Spatially resolved photocurrents in BST/GaAs and BST/Mica samples. Scanning photocurrent images of J_{C}, J_{D}, J_{L1}, and J_{L2} in BST/GaAs with a top gate at $V_{\mathrm{G}} = 0$ (a-d) and BST/Mica without a top gate (e-h), taken at $T = 30$ K. In (a), J_{C} is uniform under the gate at $V_{\mathrm{G}} = 0$ V, whereas changes sign near the edges of the channel.

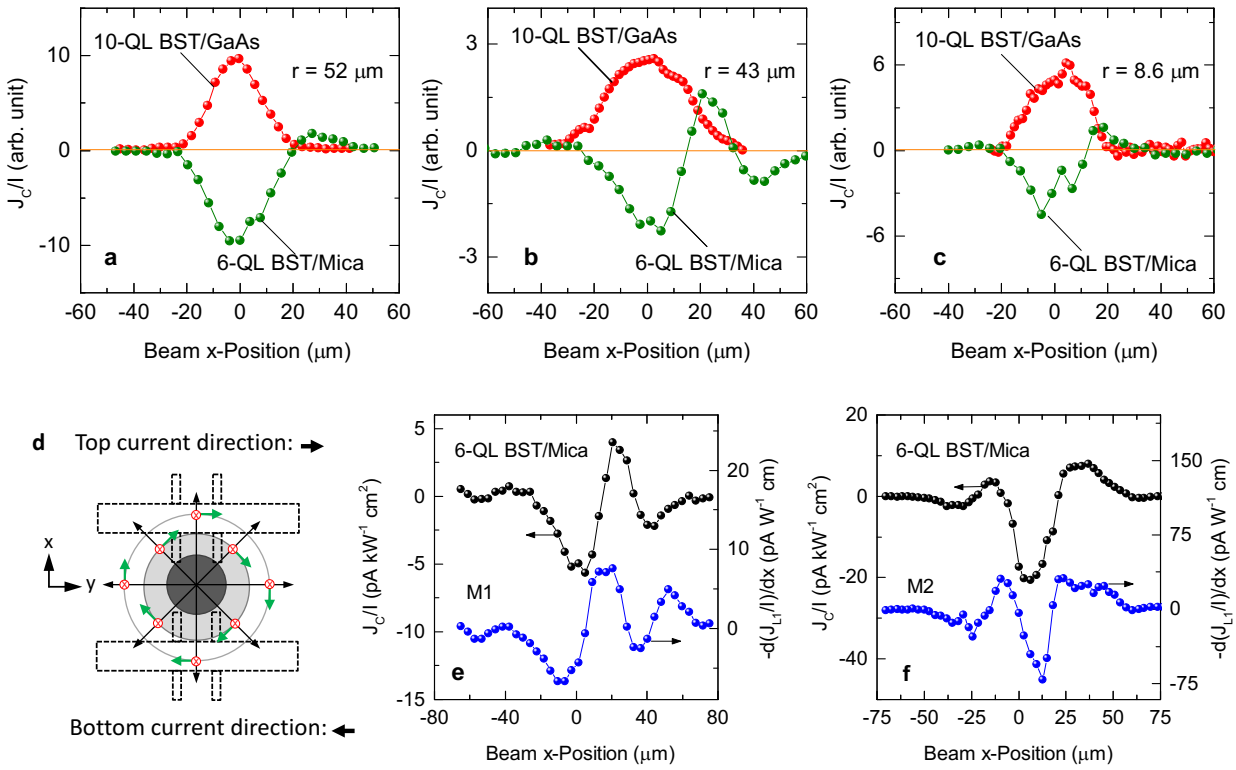

FIG. 4: Helicity-dependent photocurrent measurements in BST/GaAs and BST/Mica as a function of light spot size. (a-c) $J_{\rm C}$ along x direction in BST/GaAs (red dots) and BST/Mica (green dots), with beam radius $r = 52, 43$, and 8.6 μm. (d) Illustration of swirling current generated by a radical spin current via ISHE. Under the inclined incidence of laser beam, photo-excited electrons can possess a z component of spin polarization ($\otimes$ denotes the spin polarization direction). Due to the spatial Gaussian distribution of the laser intensity, there is a gradient in the spin density, therefore resulting in a diffused spin current flowing in the radial direction (black arrows). Consequently, a vortex charge current (grey circles) arises from the spin current via the lateral ISHE $\boldsymbol{J}_{ISHE} \propto -\boldsymbol{J}_s \times \mathbf{P}$, in which the charge current direction (green arrows) is perpendicular to both spin polarization direction ($\otimes$) and the spin current direction (black arrows). (e-f) In BST/Mica, $J_{\rm C}(x)$ follows the profile of $\frac{dJ_{\rm L1}(x)}{dx}$ in samples M1 and M2 at 296 K.

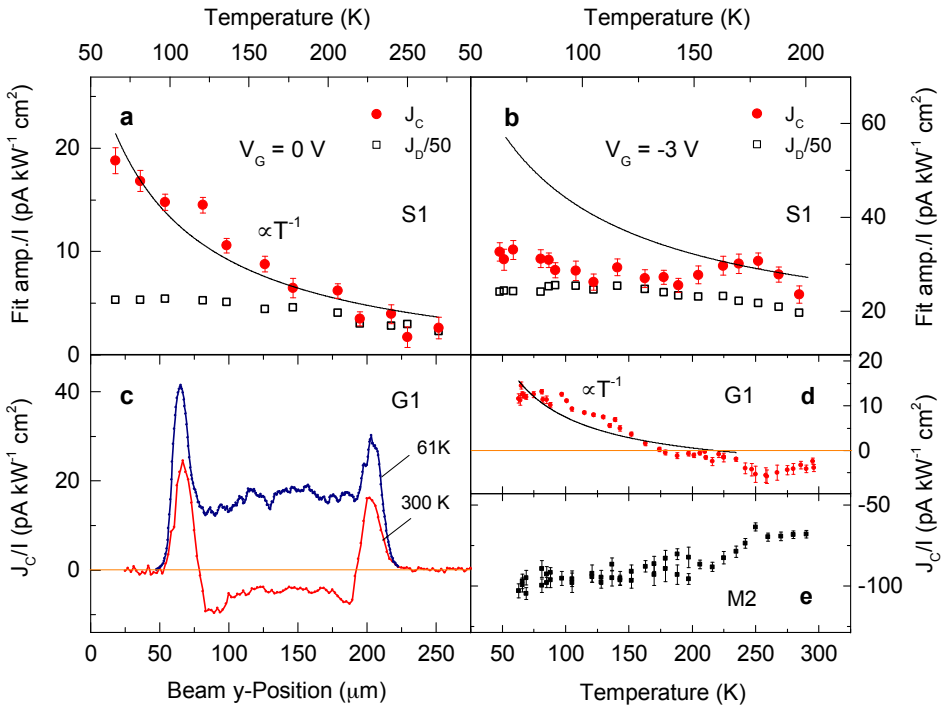

FIG. 5: Temperature dependent photocurrent measurements. (a-b) T dependence of J_C/I and J_D/I in sample S1 at $V_G = 0$ V (a) and -3 V (b). (c) J_C/I versus the beam position along y axis in sample G1 (6-QL BST/GaAs) at $T = 61$ and 297 K. (d-e) T dependence of J_C/I in BST/GaAs sample G1 (d) and BST/Mica sample M2 (e) with the same thickness $t = 6$ nm. The black curves are fit to power-law variation as T^{-1}.

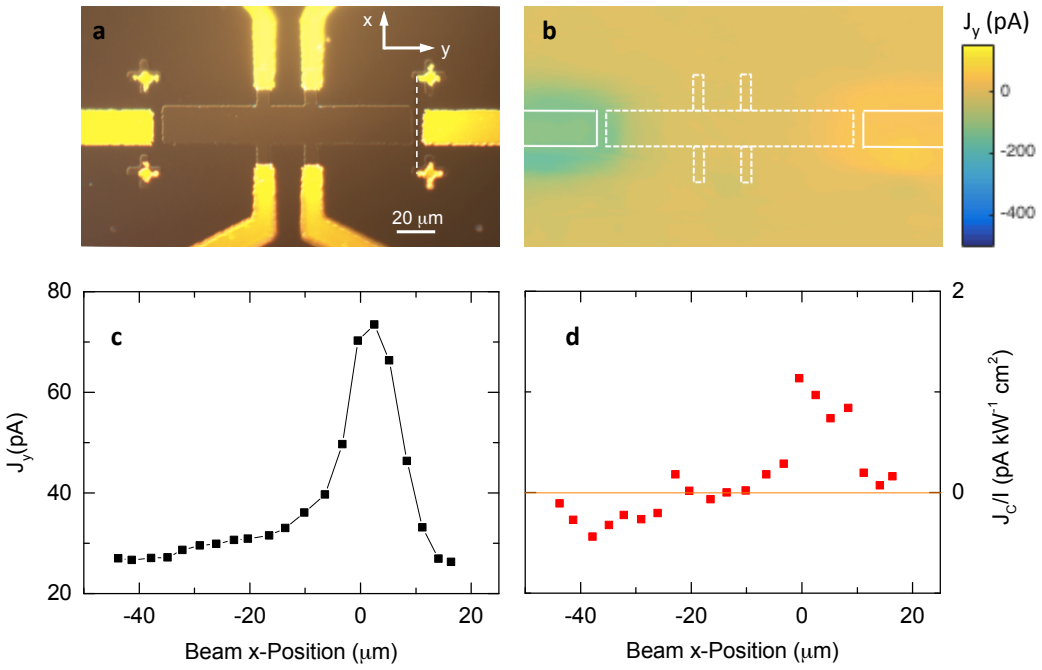

FIG. 6: Photocurrent response in the lateral GaAs-TI-GaAs sample. (a) The optical image of the GaAs-BST-GaAs sample with a 5-μm-wide window opened at each edge of the channel. (b) 2D scanning photocurrent image J_{y} excited with the linearly polarized light. Dashed and solid lines indicate the edges of the sample and electrodes, respectively. (c-d) Line scan of J_{y} at a fixed linear polarization (c) and J_{C}/I (d) as a function of beam spot position x (white dashed line in panel a) at room temperature.

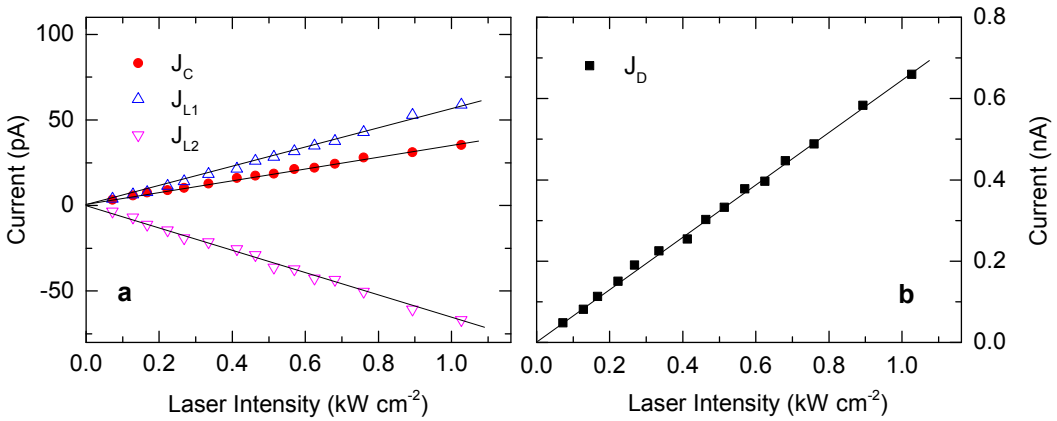

FIG. 7: The laser intensity I dependence of photocurrent at the center of the channel. (a) The extracted amplitude $J_{\rm C}$, $J_{\rm L1}$, and $J_{\rm L2}$ versus laser intensity. (b) The amplitude of the polarization independent photocurrent $J_{\rm D}$ as a function of the laser intensity. The symbols are the experimental data. The solid lines show the linear fit to the data.

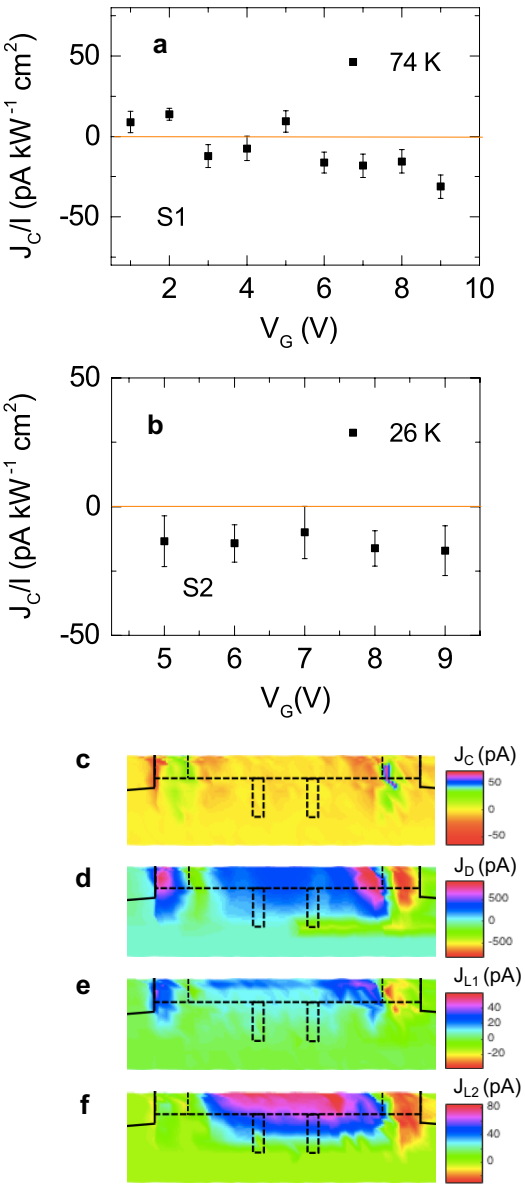

FIG. 8: (a-b) The circular photocurrent J_C/I versus gate voltage V_G in samples S1 (a) and sample S2 (b). (c-f) Scanning photocurrent current images of J_C, J_D, J_{L1}, and J_{L2} in sample S1, measured at $T = 26$ K and $V_G = 8$ V.

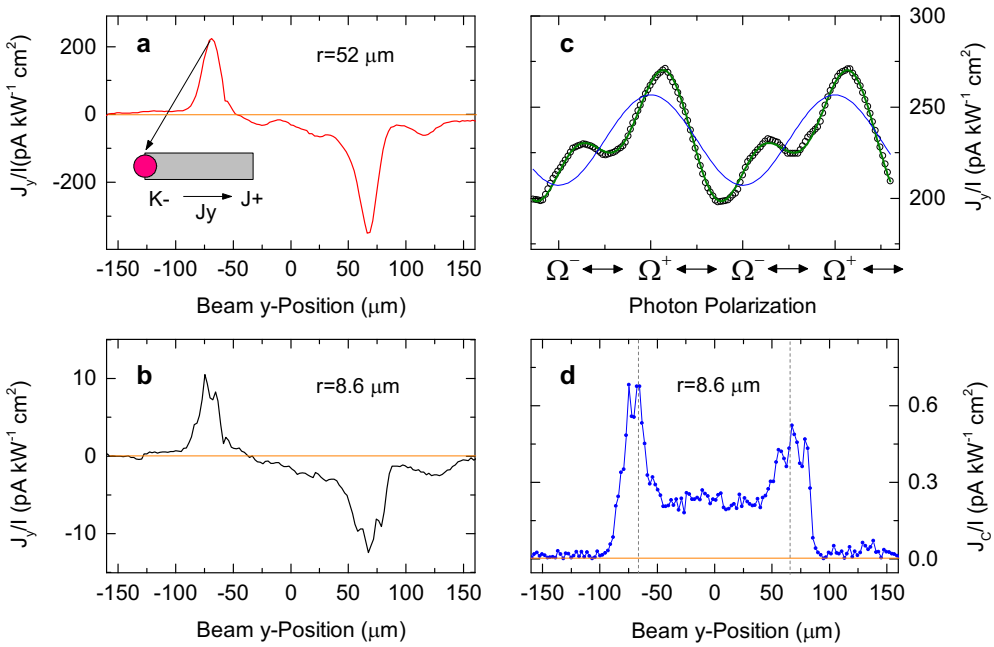

FIG. 9: Photocurrent response in the 10-QL BST/GaAs sample G2 at room temperature. (a) Line scan of $J_{\rm y}/I$ along y-axis with a beam spot radius $r = 52$ μm (half width at half-maximum). (b) The trace of photocurrent $J_{\rm y}/I$ versus photon polarization at $x = -66$ μm. The solid green line is the fit to observed data. The solid blue curve is the extracted circular photocurrent component $J_{\rm C}$. (c) Line scan of $J_{\rm y}/I$ versus y-axis with a beam spot radius $r = 8.6$ μm. (d) Line scan of $J_{\rm C}/I$ along y-axis with a beam spot radius $r = 8.6$ μm.